Reflection intensity waveform inversion

Yike Liu, Bin He, Institute of Geology and Geophysics, Chinese Academy of Sciences; Yingcai Zheng, University of Houston; Xiao-Bi Xie, University of California at Santa Cruz*

Summary

Conventional full waveform inversion (FWI) needs long offset data to update the deep structure of a velocity and low-frequency information to avoid cycle skipping with diving or refraction waves. To reduce the data requirements, we propose an approach referred to as reflection intensity waveform inversion (RIWI), which fits the difference in seismic reflection intensity between modeled and field data, so that the starting model dependence of waveform inversion can be relaxed and long offset data is no longer required. The intensity inherently has low-frequency information when compared with the original data. It can be obtained by deconstructing the intensity into low-frequency and high-frequency information using Fourier transformation. Implementing multi-scale inversions starting from low-frequency reflection intensity data can largely avoid the cycle-skipping problem. We corroborate the proposed approach validity for data without low-frequency content and long-offset information with numerical examples.

Introduction

Full waveform inversion to date has been limited to recovering shallow structures because most implementations depend heavily on diving or refracted waves (Tarantola, 1984; Luo and Schuster, 1991; Zhou et al., 2012). To mitigate the traditional limitations, reflected events were introduced for waveform inversion (Ma and Hale, 2013; Altheyab and Schuster, 2015; Chi et al., 2015; Zhang et al., 2015; Alkhalifah and Wu 2016; Martinez et al., 2016; Kazei et al., 2016; Kenneth and Warne, 2016). Xu (2012) used true amplitude migration as a reflectivity model, which could then be used to generate reflection data by de-migration. The reflection waveform inversion (RWI) gradient enabled velocity updates deeper than the maximum penetration depth of diving waves and reduced the FWI dependency on recording long offsets. The RWI algorithm implemented an approach which allowed the updating of long wavelength components of the velocity model affecting the reflected arrivals even in the absence of low-frequency information in the input data. RWI could alternatively update the background and perturbed reflectivity of a model, but could not avoid cycle skipping if no low-frequency components existed in the data or if a starting model was far from a true model.

Seismic wave intensity has different frequency characteristics. We utilize the intensity characteristics of seismic data that inherently exist in low-frequency information and build an objective function between the intensities of the reflection model data and the observed data (Liu et al., 2018). The function is optimized with respect to model parameters, where the model parameters are split into long and short wavelength components, e.g., the background model and the perturbation model. The initial background model cannot generate reflection waves, but observed data can account for reflection events. The reverse time migration (RTM) image by least square sense is used for the reflection model and then de-migration is used for generating synthetic reflection data. Near offset compared with long offset has small errors with observed data. This means travel time in near offset is almost identical for both modelled data and observed data. Intensity used for RWI will greatly reduce cycle-skipping in the absence of long offset and low frequency components.

The frequency characteristic of seismic wave intensity

The amount of energy passing through a unit area per unit of time in a specified direction is called the intensity of the wave. As the amplitude (pressure) of the seismic wave increases, the intensity of the seismic wave increases. The intensity of a seismic wave depends not only on the pressure, but also on the density and the seismic wave of the medium through which the wave is traveling. In marine environments, acquisition hydrophones are not sensitive to particle velocity and measure the pressure of a wave, rather than its intensity. The intensity is therefore calculated from the measured seismic pressure, using the relationship between the magnitude of the intensity and pressure. The wave intensity is proportional to the square of its amplitude (Born and Wolf, 1999). Unlike pressure or displacement wavefields, wave intensity has quite different frequency characteristics. The convolution of spectra of intensity causes the frequency content to split into a low- and high-frequency band (Liu et al., 2018). We illustrate a sine-based function composed of 20, 25, 27, 29 Hz to clarify the frequency differences,

10.1190/segam2018-2995832.1

$$u(t)=1.0sin(2\pi 20t)+1.0sin(2\pi 25t) +1.0sin(2\pi 27t)+1.0sin(2\pi 29t). \tag{1}$$

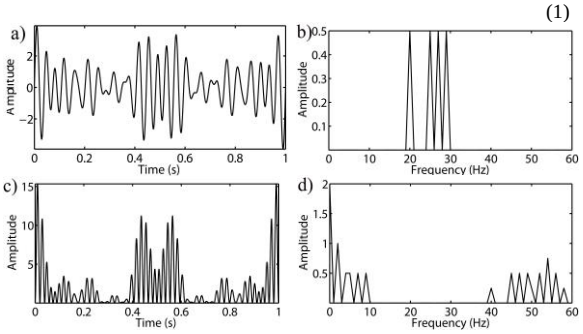

Figure 1. a) is the u(t) function composed of 20, 25, 27 and 29 Hz, respectively as shown in b); c) the intensity of u(t) which has a low-frequency part corresponding to the frequencies from 0 to 10 Hz and a high-frequency part for the frequencies from 40 to 60 Hz shown in d). There is a gap between the low-frequency and high-frequency bands in the intensity that corresponds to the original data frequency as illustrated in d).

Fréchet derivatives for RIWI with respect to velocity

We utilize the intensity characteristics of seismic data that inherently exist in low-frequency information and build an objective function between the intensities of the reflection modeled data and the observed data.

$$E(v)=\frac{1}{4}\left\|P_{cal}^2(x_r,t;x_s)-P_{obs}^2(x_r,t;x_s)\right\|_2^2, \tag{2}$$

in which objective $E(v)$ is a function of the velocity of the model, $P_{cal}^2(x_r,t;x_s)$ is the intensity of the modeled data and $P_{obs}^2(x_r,t;x_s)$ is the observed data intensity. We solve a nonlinear inverse problem by iteratively updating model parameters to minimize the difference between the modeled intensity seismic data and the observed intensity data. The derivative of the objective with respect to velocity v is given

$$\varepsilon=\frac{\partial E(v)}{\partial v}=\sum_{s,r}\int dt\,\frac{\partial P_{cal}(x_r,t;x_s)}{\partial v}P_{cal}(x_r,t;x_s) (P_{cal}^2(x_r,t;x_s)-P_{obs}^2(x_r,t;x_s). \tag{3}$$

For simplified expression, we use

$$I_{dif}(x_r,t;x_s)=(P_{cal}^2(x_r,t;x_s)-P_{obs}^2(x_r,t;x_s), \tag{4}$$

to represent the intensity difference between model data and observed data. We then derive the Fréchet derivative of the wavefield with respect to the velocity with RIWI, by splitting the model into

$$v(x)=v_0(x)+\delta v(x), \tag{5}$$

where $v_0(x)$ contains the long wavelength components of the velocity model and $\delta v(x)$ contains the short wavelength components. Accordingly,

$$P(x)=P_0(x)+\delta P(x). \tag{6}$$

By introducing the following equation (Xu et al., 2012), if we fix $\delta v(x)$, we can derive the gradient according to the background model

$$\left.\frac{\partial\delta P(x_r,t;x_s)}{\partial v_0(x)}\right|_{\delta v(x)}= \frac{2}{v_0^3(x)}\left(\frac{\partial^2 P_0(x,t;x_s)}{\partial^2 t}*\delta P(x_r,t;x)+\frac{\partial^2\delta P(x,t;x_s)}{\partial^2 t}*P_0(x_r,t;x)\right). \tag{7}$$

Substituting equation 7 into 3, we can obtain the RIWI gradient with respect to velocity:

$$\left.\frac{\partial E}{\partial v_0(x)}\right|_{\delta v(x)} =\sum_{s,r}\frac{2}{v_0^3(x)}\int dt\,\frac{\partial^2 P_0(x,t;x_s)}{\partial^2 t}\left(\delta P(x,-t;x_r)*P_{cal}(x_r,t;x_s)I_{dif}(x_r,t;x_s)\right) +\sum_{s,r}\frac{2}{v_0^3(x)}\int dt\,\frac{\partial^2\delta P(x,t;x_s)}{\partial^2 t}\left(P_0(x,-t;x_r)*P_{cal}(x_r,t;x_s)I_{dif}(x_r,t;x_s)\right). \tag{8}$$

in which $P_{cal}(x_r,t;x_s)I_{dif}(x_r,t;x_s)$ is the adjoint source and where $I_{dif}(x_r,t;x_s)$ contains the low-frequency components. Using the intensity adjoint source avoids cycle skipping by multi-scales from low to high frequencies. $\delta P(x,-t;x_r)$ means the one order perturbation of the wavefield and $-t$ means back propagated , $P_0(x,-t;x_r)$ is the backward propagated wavefield.

Marmousi example

RIWI is tested on the Marmousi model. This model consists of 496 horizontal by 176 vertical grid points with spacing of 20m in both the horizontal and vertical directions. The acquisition system includes 56 sources, evenly spaced at 180m on the top of the model. There are 150 receivers fixed on the top of the model at an interval of

10.1190/segam2018-2995832.1

20m. A sample trace with 8 Hz dominant frequency is illustrated in Figure 2, where Figure 2a is the time-domain waveform; Figure 2b is the frequency spectrum with its frequency content below 4 Hz removed; Figure 2c is the intensity of the trace; and Figure 2d shows the frequency spectrum of the intensity. Comparing Figure 2b with 2d, we see that the latter contains much lower-frequency information. To test RIWI using a reflected wave capable of handling the data without the low-frequency content, the data is filtered with a Butterworth filter at the 4-5-12-15 Hz passband.

The Marmousi model is shown in Figure 3a with the direct wave removed. In the first outer loop, in order to generate true amplitude reflection data and a reflectivity model from the smooth background velocity model (Figure 3b), we used least-squares reverse time migration (LSRTM)-based methodology to update the reflectivity model. We only used the near-offset data for the inversion, which was then iterated 10 times by LSRTM. RIWI was then conducted to calculate the gradients with all offset data. For RIWI, we calculated the data intensity and then applied a 0-0-2-4Hz band-pass filter to the intensity using reflection waves. The gradients were smoothed during the inversion by applying a scattering angle filter (Kazei et.al 2016). For the reflection part, 5 iterations were used to update the background velocity model. For the next outer loops, we first initialized the reflectivity model with LSRTM by applying the updated velocity model and near-offset observation data. After updating the reflectivity model with the updated velocity by LSRTM, the velocity was then updated according to the new reflectivity model. Each of the outer loops had the same number of iterations as the first outer loop and a total of 10 outer loops were determined. Figure 3d is the updated background velocity model.

To test the effectiveness of RIWI in constructing a background velocity model, we performed a multi-scale FWI on both the initial velocity model and the inverted background velocity model obtained by RIWI. The data was filtered using a series of pass-bands at 4-4.5, 4-6.5 4-9, 4-13 and 4-15Hz and each frequency band was iterated 30 times, for a total of 150 iterations. Figures 3c and 3e are the final results of FWI corresponding to the initial linear model and the inverted model calculated by RIWI. It can be seen that there is a serious local minima for the FWI from the linear initial model, whereas the result using the inverted background obtained by using RIWI as the initial model is greatly improved. To see more clearly the difference between using the initial model and inverted model, a vertical velocity profile is extracted at 3km from the surface. Figure 4a shows the 1-D initial model (dashed), and the result obtained using RIWI (dotted). Figure 4b compares the intermediate model from FWI with the linear increase initial model (dashed), the final result using RIWI plus FWI (dotted) and the true velocity model (solid). The dashed line shows a large error at the depth 1.0 to 1.5 km and has a big delay at the deep structure.

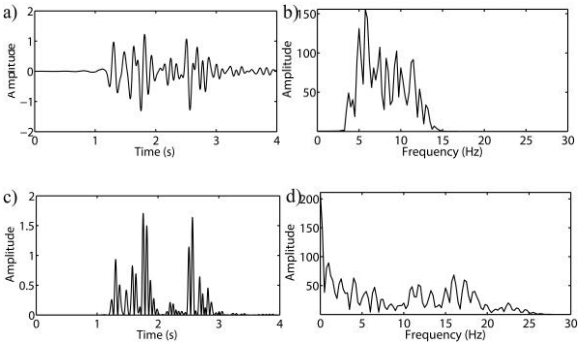

Figure: 2 For the Marmousi model: a) the time-domain trace; b) the frequency spectrum of the trace with frequency content below 5Hz removed; c) the intensity of the trace; and d) the frequency spectrum of the intensity.

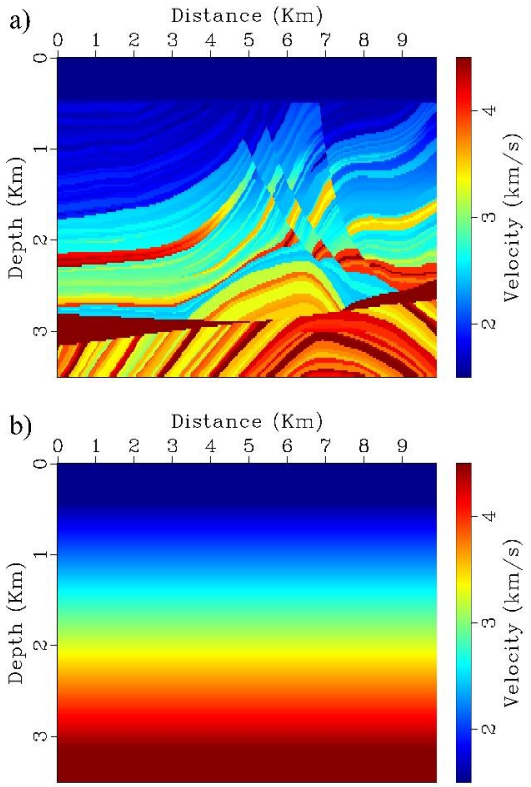

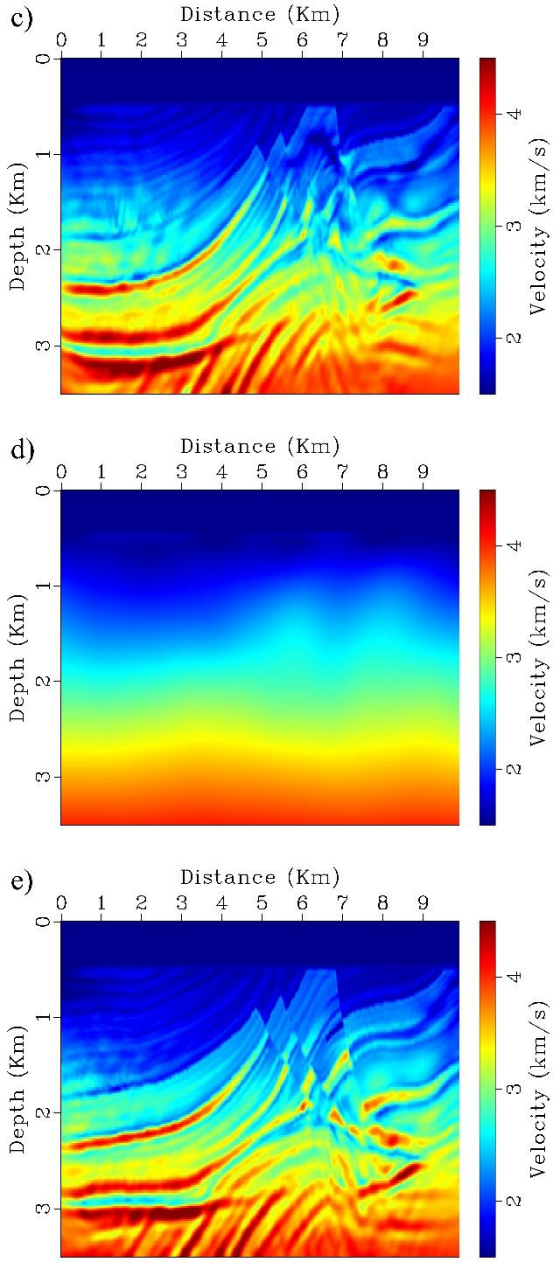

Figure:3 Results for the Marmousi model, showing a) the velocity model; b) the initial model; c) the inverted velocity model using conventional FWI; d) the inverted velocity model using RIWI; and e) the inverted velocity RIWI+FWI.

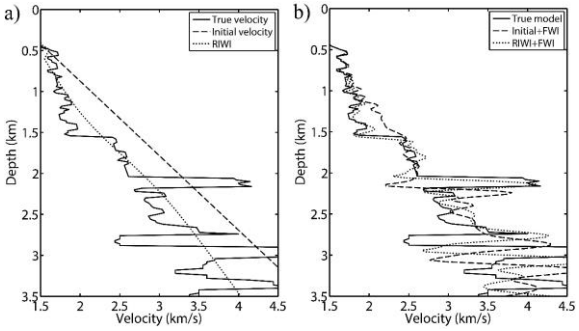

Figure: 4 (a) After updating by FIWI, the inverted initial model is closer to the average of the Marmousi model when compared with the initial linear model. (b) the dashed line shows the inverted model by multi-scale FWI with a linear increase from the initial model, and the dotted line shows the inverted model by multi-scale FWI with the RIWI result used as the initial model. The dashed line shows a large error at a depth 1.0 to 1.5 km and has a long delay in the deep structure.

Conclusions

RIWI has been developed to avoid cycle-skipping due to the data lacking low-frequency content. An analysis of the Fréchet derivatives of RIWI show that it can utilize the reflections to recover the long wavelength structure in situations where the initial model is significantly different to the true model. Numerical examples corroborate this method's ability to handle conventional reflection data.

Acknowledgements

We would like to express our sincere gratitude to Sheng Xu, Hongbo Zhou and Yi Luo for their constructive comments and helpful suggestions. This research was funded by Statoil Petroleum (Grant No. 4503288025).

10.1190/segam2018-2995832.1

REFERENCES

Altheyab, A., and G. T. Schuster, 2015, Reflection full-waveform inversion for inaccurate starting models: 85th Annual International Meeting, SEG, Expanded Abstracts, 1148–1152, https://doi.org/10.1190/segam2016-13966097.1.

Alkhalifah, T., and Z. Wu, 2016, The natural combination of full and image-based waveform inversion: Geophysical Journal International, **200**, 363–373, https://doi.org/10.1111/1365-2478.12264.

Born, M., and E. Wolf, 1999, Principles of optics, 7th ed.: Cambridge University Press.

Chi, B., L. Dong, and Y. Liu, 2015, Correlation-based reflection full-waveform inversion: Geophysics, **80**, no. 4, R189–R202, https://doi.org/10.1190/geo2014-0345.1.

Liu, Y., B. He, Z. Zhang, X. Xiao, and Y. Zheng, 2018, Full intensity waveform inversion: 88th Annual International Meeting, SEG, Expanded Abstracts.

Luo, Y., and G. T. Schuster, 1991, Wave-equation traveltime inversion: Geophysics, **56**, 645–653, https://doi.org/10.1190/1.1443081.

Martinez, R. J., S. Crawley, K. Zou, A. A. Valenciano, L. Qiu, and N. Chemingui, 2016, A robust gradient for long wavelength FWI updates: 78th Annual International Conference and Exhibition, EAGE, Extended Abstracts, https://doi.org/10.3997/2214-4609.201601536.

Kazei, V., E. Tessmer, and T. Alkhalifah, 2016, Scattering angle-based filtering via extension in velocity: 86th Annual International Meeting, SEG, Expanded Abstracts, 1157–1162, https://doi.org/10.1190/segam2016-13870908.1.

Kenneth, I., and M. Warner, 2016, Reflection FWI: 86th Annual International Meeting, SEG, Expanded Abstracts, 1136–1140, https://doi.org/10.1190/segam2016-13944219.1.

Ma, Y., and D. Hale, 2013, Wave-equation reflection traveltime inversion with dynamic warping and full-waveform inversion: Geophysics, **78**, no. 6, R223–R233, https://doi.org/10.1190/geo2013-0004.1.

Tarantola, A., 1984, Inversion of seismic reflection data in the acoustic approximation: Geophysics, **49**, 1259–1266, https://doi.org/10.1190/1.1441754.

Xu, S., D. Wang, F. Chen, G. Lambare, and Y. Zhang, 2012, Inversion on reflected seismic wave: 82nd Annual International Meeting, SEG, Expanded Abstracts, 1–7, https://doi.org/10.1190/segam2012-1473.1.

Zhang, S., Y. Luo, and G. Schuster, 2015, Shot-and angle-domain wave-equation traveltime inversion of reflection data: theory: Geophysics, **80**, no. 4, U47–U59, https://doi.org/10.1190/geo2014-0178.1.

Zhou, H., L. Amundsen, and G. Zhang, 2012, Fundamental issues in full waveform inversion: 74th Annual International Meeting, SEG, Expanded Abstracts, 1–5, https://doi.org/10.1190/segam2012-0878.1.